

The enhancement of viscous fingering with bidisperse particle suspension

Feng Xu¹ and Sungyon Lee^{1,†}

¹Department of Mechanical Engineering, University of Minnesota, Minneapolis, MN 55455, USA

(Received 18 May 2018; revised 16 September 2018; accepted 14 October 2018;
first published online 7 December 2018)

Viscous fingering is observed experimentally when a bidisperse suspension displaces air inside a Hele-Shaw cell, despite the stabilising viscosity ratio between the invading (suspension) and defending (air) phases. Careful experiments are carried out to characterise this instability by either systematically varying the large-particle concentrations ϕ_{l0} at constant total concentrations ϕ_0 , or changing ϕ_0 with fixed ϕ_{l0} . Leading to the instability, we observe that larger particles consistently enrich the fluid–fluid interface at a faster rate than small particles. This size-dependent enrichment of the interface leads to an earlier onset of the fingering instability for bidisperse suspensions, compared to their monodisperse counterpart of all small particles. In particular, even the small presence of large particles is shown to effectively lower the total particle concentration needed for fingering, compared to the all-small-particle case. We hypothesise that the key mechanism behind this enhanced viscous fingering is the size-dependent nature of shear-induced migration of particles far upstream from the interface. A reduced equilibrium model is derived based on the modified suspension balance model to verify this hypothesis, in reasonable agreement with experiments.

Key words: fingering instability, multiphase and particle-laden flows

1. Introduction

The classic viscous fingering refers to the instability at the interface between two fluids when a less viscous fluid displaces a more viscous one inside porous media (Saffman & Taylor 1958; Homsy 1987). More recently, fingering has been observed even in the absence of this destabilising viscosity ratio, when a mixture of oil and non-colloidal particles displaces air in a Hele-Shaw cell (Tang *et al.* 2000; Ramachandran & Leighton 2010; Xu, Kim & Lee 2016; Kim, Xu & Lee 2017). This so-called particle-induced viscous fingering is shown to originate from shear-induced migration of particles normal to the flow direction, which refers to the tendency of non-colloidal particles to migrate across streamlines from regions of high to low shear (Leighton & Acrivos 1987*b*; Graham *et al.* 1991; Husband *et al.* 1994; Krishnan & Leighton 1994). Once particles collect near the channel centre due to shear-induced migration, they achieve a faster average axial velocity and accrete at the advancing oil–air interface, which generates the destabilising effective viscosity gradient.

† Email address for correspondence: sungyon@umn.edu

While previous studies mostly focused on the dependence of particle-induced fingering on the particle volume fraction ϕ_0 , Kim *et al.* (2017) uncovered that fingering behaviour (i.e. finger onset and wavenumber) differs drastically between monodisperse suspensions of all small versus all large particles. Given this size-dependent behaviour of particle-induced fingering, the natural question that follows is how the inclusion of particles with two different radii in the suspension will impact fingering. In this paper, we directly address this question experimentally and theoretically by studying a bidisperse suspension that radially displaces air inside a Hele-Shaw cell. From the practical standpoint, most industrial applications with suspensions, such as coating (van der Kooij, Kassapidou & Lekkerkerker 2000) and three-dimensional (3D) printing (Chahal, Ahmadi & Cheung 2012; Connell *et al.* 2013), involve a wide distribution of particle sizes. Hence, the current study of bidisperse suspensions offers a logical first step from considering the interfacial dynamics of purely monodisperse suspensions towards more practical polydisperse mixtures.

The dynamics of bidisperse suspensions has been studied experimentally in the low-Reynolds-number regime over the past few decades (Graham *et al.* 1991; Husband *et al.* 1994; Krishnan & Leighton 1994; Krishnan, Beimfohr & Leighton 1996). For instance, Graham *et al.* (1991) employed nuclear magnetic resonance (NMR) imaging to study the migration of concentrated suspensions undergoing flow between rotating concentric cylinders. They reported that large particles in bimodal suspensions form concentric cylindrical sheets inside the Couette cell, which provided the first insight into the effects of polydispersity on shear-induced migration of particles. Husband *et al.* (1994) measured the particle migration in suspensions of bimodal spheres and showed that the coarse fraction of particles migrates much faster than the fine fraction, which leads to the size segregation of initially well-mixed suspensions. Following these studies, Lyon & Leal (1998*b*) measured the velocity and concentration profiles for bidisperse suspensions undergoing a pressure-driven flow in a rectangular Hele-Shaw cell. More recently, Norman, Oguntade & Bonnecaze (2008) reported the size segregation of bidisperse suspensions in pressure-driven pipe flows, taking into account the negative buoyancy of particles. Hence, the existing experimental studies on bidisperse suspension systems have clearly demonstrated that the effects of shear-induced migration depend on the particle size, which can lead to the size segregation of particle species in different flow geometries. The present study will add to this rich body of work on bidisperse suspensions by focusing on how this size-dependent nature of shear-induced migration may alter the particle-induced viscous fingering.

From the theoretical perspective, several continuum models have been developed to study the suspension dynamics. The first approach is called the diffusive flux model, which was originally proposed by Leighton & Acrivos (1987*b*) to explain their experimental observations (Leighton & Acrivos 1987*a*). The model is built on the conjecture that particles can migrate across streamlines in the gradient of shear, particle concentration or effective viscosity, via non-hydrodynamic interactions; the model utilises the phenomenological expression for particle diffusion that relates the resultant particle flux to the gradient of these aforementioned quantities. This model was further developed by Krishnan *et al.* (1996) to account for the effect of the streamline curvature, enabling the model to explain the lack of migration of particles in parallel-plate flow where there exists an outward-growing shear rate (Chapman 1990). Another successful method is called the suspension balance model, which was originally developed by Nott & Brady (1994) to study pressure-driven

suspension flows. Distinct from the diffusive flux model, the suspension balance model accounts for the normal components of particle phase stress that are induced by shear, and the particle migration results from the normal stress gradient. More recently, Boyer, Guazzelli & Pouliquen (2011) proposed the frictional suspension rheology to capture the transition from the fluid-like to solid-like behaviours of very dense suspensions, in excellent agreement with the experiments (Lecampion & Garagash 2014; Dagois-Bohy *et al.* 2015).

In the relatively dilute regime, both the diffusive flux model and suspension balance model have been proven to successfully capture the dynamics of monodisperse suspensions in different flow geometries (Lyon & Leal 1998*a*; Morris & Brady 1998; Morris & Boulay 1999; Murisic *et al.* 2011, 2013; Lee, Stokes & Bertozzi 2014). However, only a limited number of studies have utilised these models to describe bi- or polydisperse systems. For example, Shauly, Wachs & Nir (1998) studied the effect of particle radii on shear-induced migration in Couette flow by constructing a phenomenological model. They obtained qualitatively good agreement between the model and experimental data reported in the literature. Lyon & Leal (1998*b*) applied the suspension balance model to their bidisperse system, assuming that uniformly distributed small particles only contribute to the viscosity of the carrying fluid, and the results agreed reasonably well with their experiments. Norman *et al.* (2008) modified the suspension balance model by adding a constitutive stress equation for a second species of particles to calculate the particle concentration and corresponding velocity profiles of both particle types. No application of the frictional suspension rheology has been reported in the literature so far on polydisperse suspensions.

In this paper, we experimentally inject a bidisperse suspension to radially displace air inside a Hele-Shaw cell. The mixture consists of neutrally buoyant, non-colloidal particles (i.e. large Péclet number) with two distinct radii and viscous oil. Experimentally, we quantify the clear preferential accumulation of large particles (over smaller ones) at the fluid–fluid interface. This size-dependent particle accumulation is also shown to ‘enhance’ or expedite the onset of fingering upon the inclusion of even a small amount of large particles, compared to the monodisperse counterpart. To rationalise the experimental results, we also compute the particle concentration profiles that account for size-dependent shear-induced migration, following the theoretical framework of Nott & Brady (1994) and Norman *et al.* (2008). The comparison between the experimental measurements of the depth-averaged concentrations and the calculations shows satisfactory agreement.

This paper is organised as follows. First, § 2 consists of the description of the experimental set-up and method, followed by the results of our key experimental observations and measurements. Then, in § 3, we lay out the theoretical framework based on the suspension balance model; results from the numerical calculation and comparison to experimental measurements are also provided in this section. We conclude the paper with a brief discussion in § 4.

2. Experiments

2.1. Apparatus and procedure

The experiments are performed by radially injecting a bidisperse suspension into a Hele-Shaw cell that is open to air from all sides (see Xu *et al.* (2016) for the original set-up). The cell consists of two pieces of Plexiglas with dimensions 30.5 cm × 30.5 cm × 3.8 cm that are separated to a constant gap thickness $h = 1.40$ mm with standard shims (McMaster). There is a hole drilled at the centre

of the bottom plate, through which the suspension is injected via a clear vinyl tube at a constant flow rate $Q = 150 \text{ ml min}^{-1}$ with a syringe pump (New Era Pump Inc., NE-1010). A light-emitting diode (LED) panel (Enviroasis, 75 W, 4200 lumen) is placed under the cell to provide uniform illumination. All the experiments are recorded from the top down with a digital camera (Nikon D500) at a rate of 60 frames per second (f.p.s.).

The fluid used is polydimethylsiloxane-based silicone oil (PDMS, United Chemical), with viscosity $\eta_f = 0.096 \text{ Pa s}$ and density $\rho_f = 0.96 \text{ g cm}^{-3}$. We assume that the PDMS behaves as a Newtonian fluid given its relatively low kinematic viscosity and molecular weight (Murisic *et al.* 2013). The suspended particles are fluorescent spherical polyethylene beads (Cospheric) with density $\rho_p = 1.00 \text{ g cm}^{-3}$ and two distinct diameters. The larger (red) particles have a mean diameter of $d_l = 327 \text{ }\mu\text{m}$ (range 300–355 μm), while that of the smaller (green) ones corresponds to $d_s = 137 \text{ }\mu\text{m}$ (range 125–150 μm). The colours are specifically chosen to provide visual contrast between the two particle types. The slight mismatch between the particle and fluid densities gives rise to particle settling inside the suspension. The Stokes settling speed can be estimated as $u_s = (\rho_p - \rho_f)gd^2f(\phi)/(18\eta_f)$, where the hindrance function $f(\phi) = (1 - \phi)^{4.4}$ captures the effects of many-particle sedimentation (Altobelli & Mondy 2002; Beyea, Altobelli & Mondy 2003), and ϕ denotes the particle volume fraction. Then, based on the characteristic parameters (e.g. $\phi \sim 0.2$), the settling distance in the experimental time scale ($\sim 20 \text{ s}$) corresponds to 0.17 and 0.032 mm for large and small particles, respectively, which is much less than h . Hence, we neglect the effects of particle sedimentation in our present analysis.

For each experiment, the volumes of each component – fluid and two types of particles – are carefully measured out to set the total initial volume fraction ϕ_0 , as well as the volume fraction of each particle species: ϕ_{l0} for large and ϕ_{s0} for small particles. All the components are added and mixed together inside a syringe to achieve a uniform distribution of suspended particles. The syringe containing the suspension is left open for a sufficient amount of time to allow for trapped air bubbles to escape. The value of ϕ_0 ranges from 15% to 25% with an increment of 1%, while ϕ_{l0} is varied from 1% up to 5% at given ϕ_0 ; ϕ_{s0} is adjusted accordingly based on $\phi_0 = \phi_{l0} + \phi_{s0}$. All combinations of volume fractions used in the experiments are summarised in table 1.

2.2. Data analysis

All the videos of experiments are processed with image processing codes developed in MATLAB. In particular, we aim to extract two sets of information from each experiment: the shape and position of the evolving suspension–air interface as well as the depth-averaged concentrations of the bulk suspension (i.e. $\bar{\phi}(r)$) and of the respective particle component (i.e. $\bar{\phi}_l(r)$ and $\bar{\phi}_s(r)$) as functions of the radial position r . In terms of the interface tracking, we use the built-in edge detector in MATLAB, which takes the smoothed images using the median filter as an input. The detector utilises the ‘canny’ method to identify the maximum changes in the local intensity gradient and recognises them as the edge. On the other hand, the concentration profiles are calculated by correlating the light intensities (indicated by matrix I hereafter) to $\bar{\phi}$. However, a major challenge lies in finding a correlation between I and the concentration profiles of each particle species. To overcome this, we construct and train a classifier with an artificial neural network (ANN), which takes the RGB (red, green, blue) values of groups of pixels as an input; this allows for tracking of particles of different colours.

$\phi_0 (\times 100 \%)$	$\phi_{l0} (\times 100 \%)$
15	4, 5
16	1, 3, 4
17	1, 2, 3, 5
18	1, 2, 3, 4, 5
19	1, 2, 3
20	1, 2, 3, 5
21	1, 3
22	1, 3, 5
23	1, 3, 5
24	1, 5
25	1, 5

TABLE 1. Summary of all combinations of the concentrations (total, ϕ_0 ; and large particles, ϕ_{l0}) used. For all experimental runs, the flow rate Q and the gap thickness h are kept constant at 150 ml min^{-1} and 1.397 mm , respectively.

In the three-layer ANN built, the sigmoid function $S(x) = 1/(1 + e^{-x})$ is employed as the activation for the hidden layer, where x represents any arbitrary input from the input layer. The three-layer network is thus expressed as

$$Z_i = S \left(\sum_{j=1} w_{ij}^{(1)} x_j + w_{i0}^{(1)} \right) = S(W_i^{(1)} \mathbf{x}), \tag{2.1a}$$

$$H_{wi} = \sum_{j=1} w_{ij}^{(2)} Z_j + w_{i0}^{(2)} = W_i^{(2)} \mathbf{Z}, \tag{2.1b}$$

where Z_i is the activation acquired from the hidden layer, w_{ij} is the weight associated with the connection from the j th node to the i th node in its predecessor layer, \mathbf{W} is thus the resultant weight matrix, and H_w is the output from the output layer – see figure 1(a) for a schematic.

With the network explicitly represented above, we hereby define the following cost function applying the logistic discrimination for multi-class classification:

$$J(\mathbf{W}) = -\frac{1}{m} \left[\sum_{i=1}^m \sum_{k=1}^K y_k^{(i)} \log H_w(x_k^{(i)}) + (1 - y_k^{(i)}) \log(1 - H_w(x_k^{(i)})) \right], \tag{2.2}$$

where \mathbf{y} corresponds to the classification vector, $\mathbf{y} \in \mathbb{R}^K$, m represents the total number of training samples and K is the number of classes for the classification problem. The coefficients in \mathbf{W} are determined by minimising the cost function J , which is achieved by performing back-propagation (Alpadydin 2009). We evaluate the network by calculating the rate of correctness C as a function of number of iterations N . As shown in figure 1(b), the correctness rate stabilises at 98%, suggesting very robust performance. See appendix A for the pseudo-code utilised.

Once the classification is complete, the respective concentration profiles are acquired assuming that the ratio of the green (small-particle) to red (large-particle) area fractions is proportional to the volume fraction ratio (i.e. $\bar{\phi}_s/\bar{\phi}_l$). This ANN method has been applied to sample mixtures with known concentrations for calibration purposes (shown in appendix B). Additional details on data analysis will be given in § 2.3.

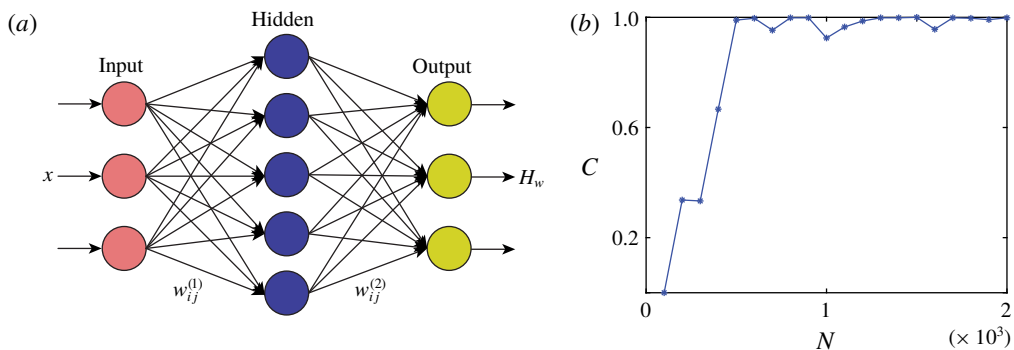


FIGURE 1. (Colour online) (a) Schematic of a three-layer ANN, which contains the input, hidden and output layers. (b) Performance of the classifier (indicated by the rate of correctness C) as a function of iteration N .

2.3. Results

2.3.1. Observations

Figure 2(a) highlights key experimental observations with two series of images. For consistency, all the images shown correspond to the time $t = 20$ s relative to t_0 that is set to the instant of the suspension's initial entry into the Hele-Shaw cell. In the top row of figure 2(a), ϕ_0 is increased from 14% to 22%, while ϕ_{10} is held constant at 5%, with two noteworthy features. First, with an increase in ϕ_0 , there are more pronounced deformations of the suspension–air interface coupled with the formation of particle clusters, which we refer to as ‘fingering’. For instance, at $\phi_0 = 5\%$, no fingering occurs at $\phi_0 = 14\%$, while clear interfacial deformations and particle clustering are evident for $\phi_0 \geq 18\%$. This ϕ_0 dependence of fingering will be quantified in § 2.3.3. Second, in all the images at $\phi_{10} = 5\%$, particles of different radii do not remain well mixed and uniform throughout. There are visibly more large (red) particles near the interface compared to small (green) ones, despite the presence of a relatively small volume of large particles in the mixture. In some cases, this demixing of particles may take place inside the injection tube before entering the cell, which will be further discussed in § 3.1.

The effect of systematically adding large particles to the mixture is illustrated in the bottom row of figure 2(a), in which ϕ_{10} ranges from 0% to 5% at constant $\phi_0 = 20\%$. In the monodisperse limit (i.e. $\phi_{10} = 0$), the suspension remains uniform throughout, with a stable circular interface. As ϕ_{10} is increased, we clearly observe the preferential accumulation of large particles on the interface even at ϕ_{10} as low as 1%. Then, for $\phi_{10} = 3\%–5\%$, the suspension–air interface exhibits fingering that grows more pronounced with higher ϕ_{10} , while ϕ_0 remains unchanged. Therefore, the addition of large particles is able to induce fingering at lower values of ϕ_0 , compared to monodisperse suspensions of small particles only.

In contrast to all-small-particle cases ($h/d_s \sim 10.2$), monodisperse suspensions with all large particles ($h/d_l \sim 4.2$) form a densely packed band on the interface at $\phi_0 = \phi_{10} = 20\%$, which subsequently breaks and causes large interfacial deformations (Kim *et al.* 2017). This so-called ‘band fingering’ is unique to $h/d \lesssim 5$ and differs from fingering in figure 2(a) with mostly small particles; additional quantitative features of band fingering are included in § 2.3.3. While increasing ϕ_{10} beyond 5% may induce band fingering in bidisperse suspensions, we are currently interested

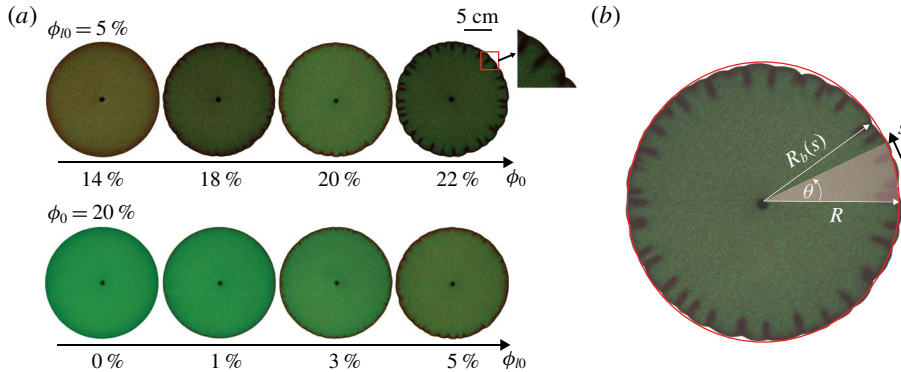


FIGURE 2. (Colour online) (a) Image sequences illustrating the effect of both ϕ_0 and ϕ_{10} in experiments with bidisperse suspensions. In the first row, $\phi_{10} = 5\%$ is held constant whereas ϕ_0 increases from 14% to 22%; in the second row, $\phi_0 = 20\%$ is kept constant while increasing ϕ_{10} from 0% to 5%. The case $\phi_{10} = 0\%$ corresponds to a monodisperse experiment, which is included for comparison. (b) In a typical image from experiment, the interface is described following a curvilinear coordinate s . The instantaneous distance from the centre of the injection hole to any arbitrary point on the interface is denoted as $R_b(s)$, and R represents the radius of the best-fitted circle out of all points along the interface. A wedge with an opening of θ is shaded here, which aids the measurement of the finger size in § 2.3.2.

in how a small amount of large particles in the mixture can influence the overall suspension dynamics. Therefore, the rest of the paper will mainly focus on quantifying and rationalising the key observations for $\phi_{10} \leq 5\%$, namely, the accumulation of large particles on the interface and resultant enhancement of fingering, compared to suspensions of small particles only.

2.3.2. Preferential particle accumulation

In order to experimentally verify the preferential accumulation of large particles at the interface, we measure the depth-averaged particle volume fractions for both the bulk suspension and the respective particle species as a function of radial position r . First, a background image is systematically subtracted from all the experimental images to eliminate any non-uniformity inherent to the experimental set-up. Then, the light intensity matrix I is extracted from the processed images to yield the depth-averaged bulk concentration $\bar{\phi}$ as follows (Shan, Normand & Peleg 1997):

$$\bar{\phi}(r) = k_1 \frac{\log \frac{I(r)}{I_{min}}}{\log \frac{I_{max}}{I_{min}}}, \tag{2.3}$$

where I_{min} and I_{max} correspond to the values of the minimum and maximum light intensity of the given image, respectively. The empirical parameter k_1 can be computed based on mass conservation; $\bar{\phi}(r)$ is integrated from the centre to the fluid interface to satisfy

$$2\pi \int_{\delta}^R \bar{\phi}(r)r \, dr = \pi\phi_0 R^2, \tag{2.4}$$

where R is the radius of the best-fitted circle to the interface, as shown in figure 2(b). Here, the lower bound of the integral δ is set to a small non-zero value, such that $0 < \delta \ll R$, to discard the region near the injection hole.

As already introduced in §2.2, an ANN has been trained to help identify and classify particles of different colours on the pixel level, which are used to find the concentration profile of each particle species. Given the classification results from the network, we are able to acquire the location of each particle type and calculate their respective area fractions $A_l(r)$ and $A_s(r)$, where the subscripts l and s indicate large and small particles, respectively. For simplicity, area fractions are assumed to scale linearly with the corresponding depth-averaged volume fractions, $A_l(r)/A_s(r) = k_2 \bar{\phi}_l(r)/\bar{\phi}_s(r)$. The empirical parameter k_2 is computed by applying mass conservation to either particle component, in addition to $\bar{\phi}(r) = \bar{\phi}_l(r) + \bar{\phi}_s(r)$.

Figure 3 shows typical profiles of the depth-averaged concentrations for $\phi_{l0} = 3\%$ (figure 3a,c) and $\phi_{l0} = 5\%$ (figure 3b,d) at time $t = 20$ s. The error bars account for uncertainties associated with extracting I , I_{min} and I_{max} from the processed images. Based on the error estimate in all three intensity values, we compute the overall margin of error for $\bar{\phi}$ in (2.3), using the standard method for error propagation (Beckwith & Marangoni 1993). In all plots displayed, $\bar{\phi}$ is observed to decrease slightly upon the entrance into the cell. It plateaus at a value lower than ϕ_0 before rising above ϕ_0 further downstream, indicating the occurrence of particle accumulation at the interface. The rise in $\bar{\phi}$ is notably higher for $\phi_{l0} = 5\%$ than for $\phi_{l0} = 3\%$. More importantly, this increase in $\bar{\phi}$ directly parallels that in $\bar{\phi}_l$, while $\bar{\phi}_s$ remains relatively flat for both plots or even decreases slightly near the interface for $\phi_{l0} = 5\%$.

This striking difference in behaviour between large and small particles leads to two key results. First, as evident in figure 2, the accretion of particles on the interface is mostly caused by large particles. Therefore, injecting more large particles (increasing ϕ_{l0}) directly leads to more particles that accumulate on the expanding interface, even if ϕ_0 remains unchanged. Second, the presence of large particles in the mixture appears to ‘shield’ small particles from reaching the interface. This is evident from comparing the plot of $\bar{\phi}(r)$ in the monodisperse suspension of all small particles (inset of figure 2), which exhibits a rise towards the interface. We will provide further explanation regarding those observations in §3.

2.3.3. Interfacial deformations – fingering

In order to quantify the fingering phenomenon in a more systematic way, we measure the deformations of the fluid–fluid interface. As illustrated in figure 2(b), s refers to the curvilinear coordinate defined tangent to the edge, and $R_b(s)$ represents the instantaneous distance between the centre of the cell and any arbitrary point on the interface. Then, we apply a ‘wedge’-shaped mask of an opening angle θ on the image and identify the local maxima and minima in $R_b(s)$ within the masked segment (see figure 2b). The difference between each pair of local extrema (i.e. $\max(R_b) - \min(R_b)$) is further defined as λ , which roughly corresponds to the length of the interfacial finger. Considering that there are on average 40–50 fingers in the fingering regime, we specifically choose $\theta = 15^\circ$ so that the corresponding mask covers at most two consecutive fingers, if any. Subsequently, the mask is rotated at a fixed increment about the centre to scan the entire interface and to yield a series of λ values. The average of all λ values, or $\bar{\lambda}$, represents the overall deformation of the suspension–air interface.

The time evolution of $\bar{\lambda}$ exhibits a couple of characteristic behaviours that are currently not well understood. First, for $\phi_0 \leq 20\%$ and $\phi_{l0} \leq 5\%$, $\bar{\lambda}$ appears to grow

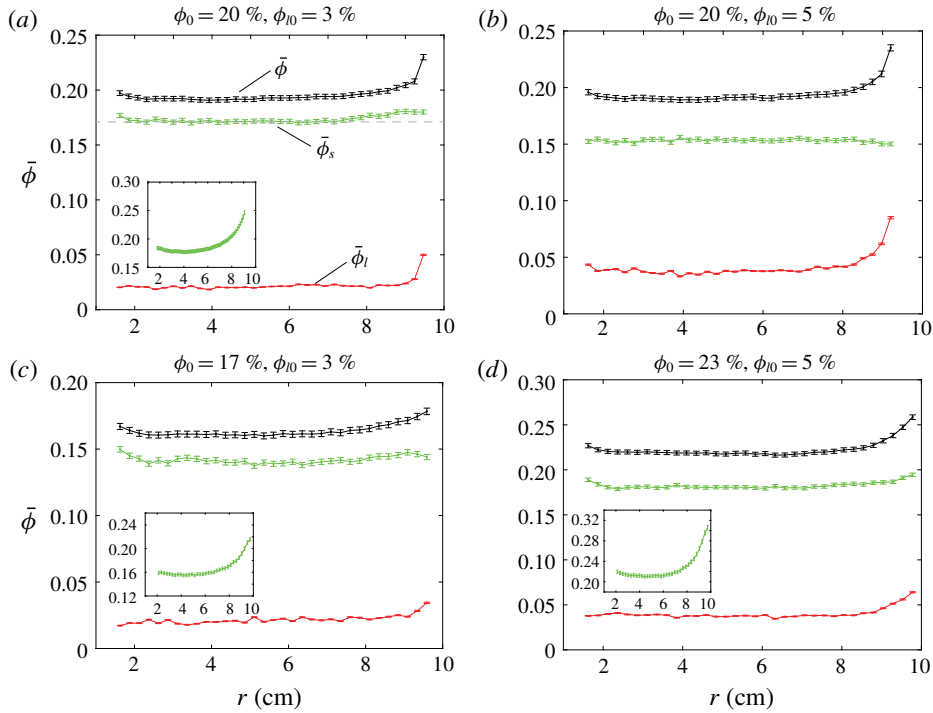


FIGURE 3. (Colour online) The depth-averaged concentration profiles as a function of radial position acquired for different combinations of ϕ_0 and ϕ_{10} at $t = 20$ s. In (a–d), $\bar{\phi}$ experiences a slight drop upon entrance into the cell and remains relatively flat in the region away from the interface. There is a clear rise in $\bar{\phi}$ towards the interface, indicating the occurrence of particle accumulation. The preferential accumulation of large particles is evident when comparing the profiles of $\bar{\phi}_s$ and $\bar{\phi}_l$. The corresponding $\bar{\phi}$ profiles from monodisperse experiments at the same ϕ_0 are also included as insets. Comparison between the mono- and bidisperse $\bar{\phi}_s$ suggests that the accumulation of small particles near the interface in the bidisperse suspension is suppressed.

linearly with time with a slope that increases with ϕ_0 and ϕ_{10} (see figure 4a,b), while $R(t) \propto t^{-1/2}$. Second, as shown in figure 4(b), when $\phi_0 > 20\%$ and $\phi_{10} = 5\%$, $\bar{\lambda}$ increases nonlinearly with t and even plateaus to a constant value at $\phi_0 = 22\%$. Finally, for a monodisperse mixture of all large particles (i.e. $\phi_0 = \phi_{10} = 20\%$), $\bar{\lambda}$ grows steeply with time in figure 4(a) before reaching a local peak around $t \approx 5$ s; this corresponds to the instance of the particle band breakup (Kim *et al.* 2017). Qualitatively, we conjecture that the growth rate of $\bar{\lambda}$ must be set by the interplay between the destabilising viscosity gradient due to particle accumulation and the stabilising effects of surface tension. However, a quantitative analysis remains outside the scope of this paper. For instance, modelling $\bar{\lambda}(t)$ and emergent finger structures involves a detailed stability analysis and a description of the complete base flow. The development of the base flow model is still under way, as it must combine the quasi-fully developed flow far upstream and the complex secondary flow near the interface, known as a ‘fountain flow’ (Karnis & Mason 1967).

Overall, $\bar{\lambda}$ is only millimetric in magnitude, as the interfacial fingers that emerge are consistently small for all the parameters considered. Also, as evident in the images

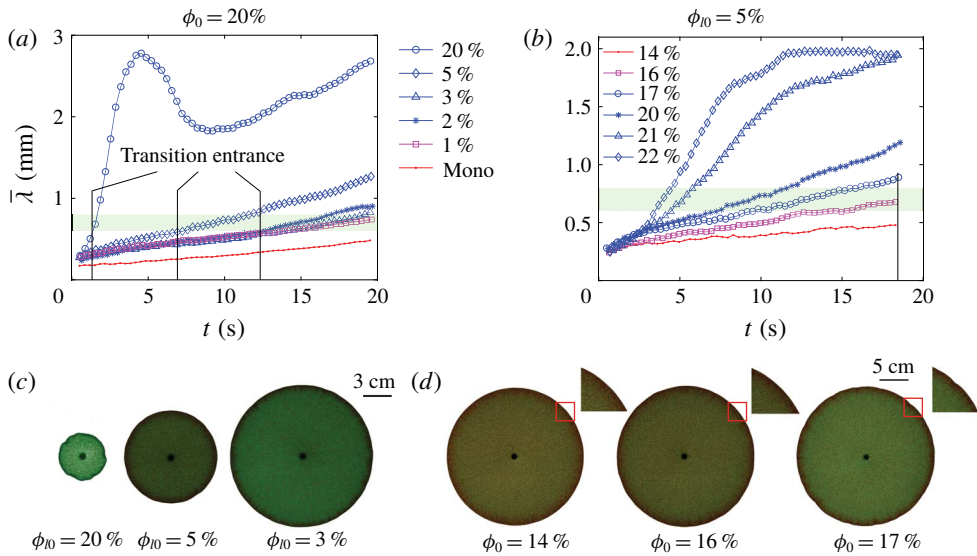


FIGURE 4. (Colour online) (a) Evolution of finger size $\bar{\lambda}$ over time for different experiments at $\phi_0 = 20\%$. The transition region from ‘no fingering’ to ‘fingering’ is shaded in green. Clearly increase in ϕ_{10} leads to growth in finger size. (b) The plot of $\bar{\lambda}$ versus time for different values of ϕ_0 at fixed $\phi_{10} = 5\%$. (c) Comparison of images from $\phi_{10} = 20\%$, 5% and 3% upon entrance into the transient region, as indicated by the vertical line in (a). (d) Images acquired at the same time at fixed $\phi_{10} = 5\%$, as indicated by the vertical line in (b). Each image represents a different regime: no fingering, transient and fingering. Zoomed-in images of the interface are included to show the difference in particle distribution as well as the interfacial deformation.

in figure 2, the fingering onset is accompanied by the emergence of particle clusters near the interface in addition to interfacial deformations, which is not captured by $\bar{\lambda}$ alone and needs to be visually verified. Hence, by carefully going through all the experimental videos, we have determined the fingering regime to initiate when $\bar{\lambda}$ reaches a threshold value between 0.6 and 0.8 mm. In figure 4(a,b), this threshold range is shaded in green to indicate the ‘transition’ from no fingering to fingering. However, it is important to acknowledge that the present analysis of fingering regimes is limited by the time scale set by the flow rate Q and the size of the cell. Owing to the time-dependent nature of $\bar{\lambda}$, even $\bar{\lambda}$ curves that stay below the threshold in the current set-up may eventually enter the fingering regime if given more time.

Figure 4(a) consists of $\bar{\lambda}(t)$ plots for constant $\phi_0 = 20\%$, while ϕ_{10} ranges from 0% to 5%. Based on the aforementioned threshold for fingering, the monodisperse case of all small particles does not finger within the current experimental set-up, while all the non-zero ϕ_{10} cases do. More importantly, even an incremental increase in ϕ_{10} is shown to expedite the onset of fingering. In figure 4(c), the experimental images at the onset (or when $\bar{\lambda} \approx 0.6$ mm) confirm that the particle accumulation at the interface and the corresponding interfacial deformations occur at an earlier time, or equivalently at a smaller radius, for $\phi_{10} = 5\%$ compared to 3% . When ϕ_{10} is held constant at 5% , figure 4(b) demonstrates that the transition to fingering is observed around $\phi_0 = 16\%$, as ϕ_0 is varied from 14% to 22% . Accordingly, figure 4(d) shows final images of three different experiments: $\phi_0 = 14\%$ (left – no fingering), $\phi_0 = 16\%$

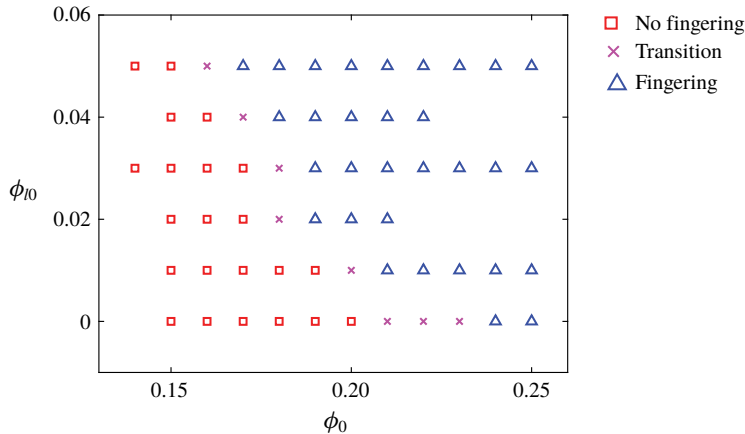


FIGURE 5. (Colour online) The phase diagram summarising the classification of different experiments into ‘fingering’, ‘no fingering’ or ‘transition’ regimes. The transition between fingering and no fingering is observed to go through a consistent shift to the lower end in terms of ϕ_0 with the increase in ϕ_{10} , suggesting that the addition of large particles in the bidisperse experiments can induce fingering at lower bulk concentrations.

(center – transition to fingering) and $\phi_0 = 17\%$ (right – fingering). As previously mentioned, while the difference in $\bar{\lambda}$ between fingering and no fingering is minimal, what sets them apart is the formation of particle clusters near the interface (see the inset), which becomes increasingly more pronounced at $\phi_0 = 17\%$.

Based on the trend in $\bar{\lambda}$, we systematically determine fingering regimes and summarise them in the ϕ_{10} – ϕ_0 phase diagram in figure 5. The squares and triangles represent the ‘no fingering’ and ‘fingering’ regimes, respectively, while the crosses correspond to the transition between the two. Clearly, there is a consistent shift of the transition regime to smaller ϕ_0 with ϕ_{10} , and this shift increases with the increase in ϕ_{10} . For example, the transition from ‘no fingering’ to ‘fingering’ occurs at $\phi_0 = 16\%$ with the initial large-particle concentration at 5%, compared to the transition at $\phi_0 = 22\%$ in the monodisperse limit. Therefore, even the small addition of large particles in the bidisperse experiments is effective in lowering the total mixture concentration ϕ_0 required for fingering. Analogously, for given ϕ_0 , the inclusion of large particles expedites the time of fingering onset, so that fingering is observed within the time scale of our current experiments.

3. Theory

3.1. Fingering mechanism

The particle-induced viscous fingering is a result of particle accumulation at the fluid–fluid interface (Tang *et al.* 2000; Ramachandran & Leighton 2010; Xu *et al.* 2016; Kim *et al.* 2017). Specifically, fingering is shown to depend directly on the amount of particles that accumulate on the advancing interface (Xu *et al.* 2016). Then, a resultant higher particle concentration near the interface corresponds to a higher local effective viscosity. This leads to miscible fingering and inhomogeneous particle distribution, or the formation of particle clusters, along the interface, as illustrated in figure 6(c). Subsequently, the suspension–air interface deforms due to the greater flow resistance of clusters compared to that of the surrounding medium.

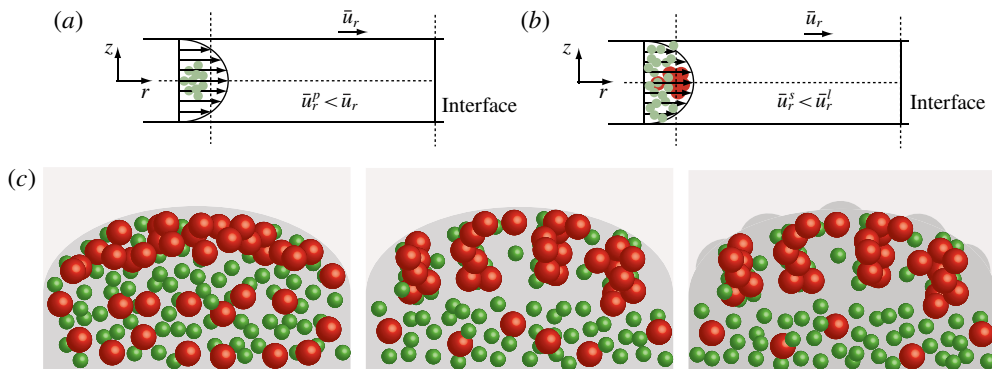


FIGURE 6. (Colour online) (a) Schematic side view of the suspension flow. Particles in the monodisperse suspension will gather near the centreline due to shear-induced migration and acquire a higher average velocity than the bulk flow. (b) In the bidisperse suspension, particles with larger diameter collect near the centreline of the channel while the distribution of small particles is relatively uniform across the channel. (c) Schematics showing the evolution of the preferential accumulation of large particles on the interface (left), the occurrence of miscible fingering (middle) and the interfacial deformations (right).

The physical mechanism behind particle accumulation is shear-induced migration of particles in the thin gap. Shear-induced migration (Leighton & Acrivos 1987*b*) refers to the migration of non-colloidal particles from high- to low-shear regions, i.e. from near the wall ($z = \pm h/2$), where particles are more likely to collide, to the centreline of the channel ($z = 0$) in this case. In the monodisperse case, depicted in figure 6(a), shear-induced migration in the z -direction yields a faster average particle velocity in the r -direction than that of the bulk suspension, such that $\bar{u}_r < \bar{u}_r^p$ (see schematic in figure 6(a)). Then, the resultant net flux of particles towards the advancing interface leads to an accretion of particles there.

Shear-induced migration also holds for bidisperse suspensions, but in a particle size-dependent manner, as previously reported by Graham *et al.* (1991), Husband *et al.* (1994), Chow, Hamlin & Ylitalo (1995) and Lyon & Leal (1998*b*). As the rate of migration is proportional to the particle diameter squared (Snook, Butler & Guazzelli 2016), the ratio of migration rates between large and small particles must be $(d_l/d_s)^2 \approx 6$. Hence, large particles collect at the centreline faster and screen out small particles. Then, the resultant average velocity of large particles is greater than that of small ones, or $\bar{u}_r^s < \bar{u}_r^l$ (see figure 6(b)), leading to a higher net flux of large particles towards the interface. Hence, as shown in figure 3, even a small addition of large particles in the bidisperse mixture prevents small particles from accumulating at the interface by suppressing their migration to $z = 0$, in clear contrast to the monodisperse case with all small particles (inset). The uniform small-particle concentration $\bar{\phi}_s$ and the rise in $\bar{\phi}_l$ are directly evident in our experiments and also consistently follow from the observations by Lyon & Leal (1998*b*).

It is important to acknowledge that particles may migrate towards the channel centre and accumulate on the advancing meniscus inside the injection tube, as previously observed by Ramachandran & Leighton (2007) and Kim *et al.* (2017). Consistent with that physical picture, the concentration profiles at early times reveal a slight rise towards the interface for different values of ϕ_0 and ϕ_{l0} (see figure 12 in appendix C). However, this enrichment effect inside the tube is minimal in comparison

to the gradual particle accumulation on the interface inside the Hele-Shaw cell. Therefore, we presently neglect the non-uniform injection conditions that may arise from shear-induced migration of particles inside the tube.

3.2. Suspension balance model for bidisperse suspensions

We model the problem as a radially expanding thin-film flow of a bidisperse suspension between parallel plates, which consists of viscous oil and non-colloidal neutrally buoyant particles. The viscous liquid is assumed to be Newtonian and incompressible, and the particles are rigid regardless of their size. We primarily focus on the region that is far upstream of the suspension–air interface, so that we can assume a quasi-fully developed uniaxial flow (Xu *et al.* 2016). Our continuum model is based on the well-established suspension balance model (Nott & Brady 1994), which has been carefully modified to account for bidisperse suspensions following the work of Norman *et al.* (2008).

We consider the mass and momentum conservation of the bulk suspension in the inertialess limit,

$$\nabla \cdot \mathbf{u} = 0, \tag{3.1a}$$

$$\nabla \cdot \boldsymbol{\Sigma} = 0, \tag{3.1b}$$

in addition to the mass and momentum conservation for each particle component,

$$\frac{\partial \phi_i}{\partial t} + \nabla \cdot (\phi_i \mathbf{u}_i^p) = 0, \tag{3.2a}$$

$$\nabla \cdot \boldsymbol{\Sigma}_i^p + \mathbf{F}_i = 0, \tag{3.2b}$$

where the subscript i corresponds to either l for large particles or s for small, respectively. In addition, the superscripts or subscripts f and p are used to differentiate between quantities corresponding to suspending fluid and particles. In the equations above, $\mathbf{u} = (u_r, u_\theta, u_z)$ and $\boldsymbol{\Sigma}$ represent the velocity vector and stress tensor in the cylindrical coordinate system, respectively. The inner drag force is given by $\mathbf{F}_i = -18\eta_f \phi_i (\mathbf{u}_i^p - \mathbf{u}) / (d_i^2 f(\phi))$, with η_f being the viscosity of the suspending fluid and the hindrance function, $f(\phi) = (1 - \phi)^{4.4}$ (Altobelli & Mondy 2002; Beyea *et al.* 2003).

The constitutive relationships relating stress tensors to the strain rate tensor \mathbf{E} and pressure p are as follows:

$$\boldsymbol{\Sigma}_i^p = 2\eta_f (\hat{\eta}_s - 1) \frac{\phi_i}{\phi} \mathbf{E} + \boldsymbol{\Sigma}_{n_i}^p, \tag{3.3}$$

$$\boldsymbol{\Sigma} = -p\mathbf{I} + 2\eta_f \mathbf{E} + \boldsymbol{\Sigma}_l^p + \boldsymbol{\Sigma}_s^p, \tag{3.4}$$

where $\boldsymbol{\Sigma}_{n_i}^p$ pertains to the normal stress tensor for each particle component. Here, the shear viscosity of the suspension (Storms, Ramarao & Weiland 1990; Shapiro & Probstein 1992) corresponds to

$$\hat{\eta}_s = \left[1 + \frac{\alpha\phi}{1 - \frac{\phi}{\phi_m}} \right]^{3.3\phi_m}, \tag{3.5}$$

where the value of the empirical parameter α depends on the particle size ratio and the volume fraction of the particle of smaller radii (i.e. ϕ_s), and ϕ_m corresponds to the maximum packing fraction of particles. In this study, considering the particle sizes in the bidisperse suspension, the values of the aforementioned parameters are chosen as $\alpha = 0.92$ and $\phi_m = 0.74$, respectively (Storms *et al.* 1990). In addition, far upstream from the interface, the flow can be considered quasi-fully developed, so that the fluxes of the suspension and the particle phases must match the constant injection conditions at the inlet:

$$Q = 2\pi r \int_{-h/2}^{h/2} u_r \, dz, \tag{3.6a}$$

$$Q\phi_{i0} = 2\pi r \int_{-h/2}^{h/2} u_{r,i}^p \phi_i \, dz. \tag{3.6b}$$

We now non-dimensionalise our governing equations and boundary conditions, based on the following scales:

$$r^* = r/R_0, \quad z^* = z/h, \quad u_r^* = u_r/U_0, \quad u_\theta^* = u_\theta/U_0, \quad u_z^* = u_z/(\epsilon U_0), \tag{3.7a-e}$$

$$t^* = tU_0/R_0, \quad \dot{\gamma}^* = \dot{\gamma}h/U_0, \quad \Sigma^* = \Sigma h/(\eta_f U_0), \quad P^* = p(\epsilon h)/(\eta_f U_0), \tag{3.7f-i}$$

where $R_0 \sim 10$ cm is the characteristic radial length scale, and $h = 1.40$ mm is the constant channel gap thickness. Hence, $\epsilon = h/R_0 \sim 0.01$ is a small parameter appropriate for lubrication approximations. The characteristic velocity U_0 is then given by $Q/(2\pi R_0 h)$. All the equations henceforward are dimensionless, unless stated otherwise, and we drop the asterisk for brevity.

By rearranging (3.2b) and combining it with the expression for F_i , we obtain the dimensionless particulate velocity,

$$\mathbf{u}_i^p = \frac{d_i^2}{18h^2} \frac{f(\phi)}{\phi_i} \nabla \cdot \Sigma_i^p + \mathbf{u}. \tag{3.8}$$

Further substitution into (3.2a) yields the following particle transport equation to the leading order in ϵ :

$$\frac{\partial \phi_i}{\partial t} + \mathbf{u} \cdot \nabla \phi_i = \frac{d_i^2}{18h^2 \epsilon} \frac{\partial}{\partial z} \left[f(\phi) \frac{\partial}{\partial z} \left(\hat{\eta}_n \dot{\gamma} \frac{\phi_i}{\phi} \right) \right]. \tag{3.9}$$

Here $\hat{\eta}_n = (\phi/\phi_m)^2 K_n \hat{\eta}_s$ is the dimensionless normal viscosity of the suspension; and $K_n = 0.75$ is an empirical constant (Norman *et al.* 2008). In particular, the transient term in (3.9) scales as $(d_i/h)^2$, which suggests that large particles must reach equilibrium due to shear-induced diffusion a factor of 6 faster than small particles (Snook *et al.* 2016). Hence, as previously noted, more large particles must be located near the channel centre $z = 0$ in the quasi-steady state and achieve a greater average radial velocity.

In order to simplify the analysis, we presently focus on the regime in which particles locally reach equilibrium in the z -direction due to shear-induced migration (Murisic *et al.* 2013). Combined with the continuum limit ($d_i \ll h$), the equilibrium condition requires that $\epsilon \ll (d_i/h)^2 \ll 1$, so that we may neglect the left-hand side

of (3.9). In a typical experiment, the particle diameters are $d_s = 137.5 \mu\text{m}$ and $d_l = 325 \mu\text{m}$, respectively, so that $(d_s/h)^2 \sim O(10^{-2})$ and $(d_l/h)^2 \sim O(10^{-1})$, while $\epsilon \sim 0.01$. Hence, we would argue that the equilibrium condition may be appropriate for the large particles but clearly breaks down for the small ones. In addition, the continuum assumption for large particles may not be completely valid, as $d_l/h \sim 0.21$. Despite these limitations, let us presently carry on with the equilibrium assumption in the manner of Murisic *et al.* (2011, 2013); we will later address the discrepancies of the model assumptions.

Once the left-hand side of (3.9) vanishes under the equilibrium condition, we integrate the right-hand side with respect to z and apply the symmetry boundary condition (i.e. $\dot{\gamma}|_{z=0} = 0$) to obtain the following equation:

$$\frac{\partial}{\partial z} \left(\hat{\eta}_n \dot{\gamma} \frac{\phi_i}{\phi} \right) = 0, \tag{3.10}$$

where the leading-order shear rate corresponds to $\dot{\gamma} = \partial u_r / \partial z$ in the lubrication limit. Physically, equation (3.10) suggests that, under shear-induced migration, both particle components rearrange themselves in such a way that the particulate normal stress is constant in the z -direction. Similarly, under the same lubrication and equilibrium assumptions, the reduced momentum equations for the suspension are given by

$$\frac{\partial P}{\partial r} = \frac{\partial}{\partial z} (\hat{\eta}_s \dot{\gamma}), \quad \frac{\partial P}{\partial z} = 0. \tag{3.11a,b}$$

Integrating both sides of the r -momentum equation with respect to z yields

$$\frac{dP}{dr} z = \hat{\eta}_s \dot{\gamma}, \tag{3.12}$$

once the symmetry condition at the centreline (i.e. $\dot{\gamma}|_{z=0} = 0$) has been applied. Finally, we arrive at the following ordinary differential equation for each particle species by combining (3.10) and (3.12):

$$\frac{\hat{\eta}_n \phi_i}{\hat{\eta}_s \phi} z = \hat{\eta}_n \dot{\gamma} \frac{\phi_i}{\phi} \left(\frac{dP}{dr} \right)^{-1} = \text{const.}, \tag{3.13}$$

which can be solved numerically subject to the fixed injection rate and input particle concentrations (3.6).

The system of equations described by (3.13) and (3.6) is highly coupled, given that $\phi = \phi_s + \phi_l$. Interestingly, Lyon & Leal (1998b) experimentally showed that the small-particle concentration remains uniform across the gap and successfully incorporated the uniform ϕ_s assumption into their mathematical model. Following their work, we will presently assume that small particles remain uniformly dispersed (i.e. $\phi_s = \phi_{s0}$) and only impact the effective viscosity of the background suspending fluid. Our experimental measurement of the depth-averaged particle concentrations in figure 3 also supports the hypothesis that small particles remain uniform throughout the expanding suspension. In addition to decoupling the equations, this assumption allows us to work around the breakdown of the equilibrium condition for small particles (i.e. $\epsilon \ll (d_i/h)^2 \ll 1$). The failure of small particles to meet the equilibrium condition is thus circumvented by assuming the uniform distribution of small particles in the bidisperse suspension.

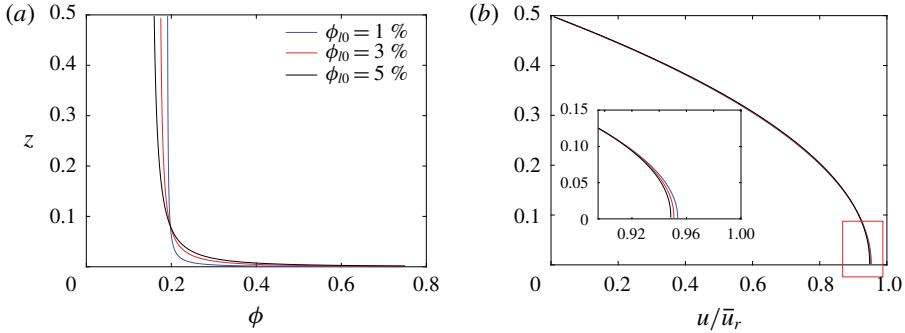


FIGURE 7. (Colour online) (a) The distribution of particles at $\phi_0 = 20\%$ with ϕ_{10} increasing from 1% to 5%. Shear-induced migration is evident with concentration increases from the near-wall region to the centreline for all cases. (b) The corresponding normalised velocity profiles are presented. The classic bluntness of the velocity profile near the centreline is observed. The inset shows the zoomed-in view of the blunted region, indicating that the increase in ϕ_{10} leads to more blunted velocity profile.

The results of our simplified equilibrium model are shown in figure 7. For $\phi_0 = 20\%$ and ϕ_{10} ranging from 1% to 5%, the total particle concentration $\phi(z)$ and corresponding axial velocity profiles are plotted along the z -axis. As expected, all three $\phi(z)$ plots in figure 7(a) show a monotonic increase from the wall ($z = 0.5$) towards the centre ($z = 0$) due to shear-induced migration; this increase is notably greater for higher values of ϕ_{10} . Here, $\phi'(z)$ appears discontinuous at $z = 0$, where the prime denotes the derivative with respect to z . This discontinuity in $\phi'(z)$ is the byproduct of the suspension balance model that caps ϕ off at ϕ_m as ϕ diverges with the vanishing local shear rate. Owing to the presence of particles, the velocity profiles are no longer parabolic but exhibit a blunted tip at $z = 0$, as shown by the plot of the normalised velocity in figure 7(b). The inset includes the zoomed-in plot of the velocity tip that becomes more blunted with an increase in ϕ_{10} .

3.3. Comparisons to experiments

Since our model is only applicable to the quasi-steady flow far upstream, it cannot quantitatively describe the fingering behaviour at the interface for varying ϕ_0 and ϕ_{10} . However, the model should be able to capture the particle accretion dynamics towards the interface, which originates from shear-induced migration of particles upstream. Based on that, we will also consider the connection between the total amount of accumulated particles and the enhanced fingering upon the addition of large particles.

Let us first test the validity of our reduced model against the measurable quantities in the experiments. For instance, figure 3 consists of the depth-averaged concentration profiles that are extracted from the experiments at time $t = 20$ s. Presently, we are unable to measure $\phi(z)$ experimentally, due to the lack of visualisation tools. Replotting $\bar{\phi}$ at different times in figure 8(a) illustrates that the curves collapse when r is normalised by the location of the interface $R(t)$ at the given time. We hereby define the upstream region as the portion of the collapsed curve that remains relatively flat, or $0 < r < R_i(t)$, where $R_i(t)/R(t)$ appears time-independent. Then, we extract the corresponding value of $\bar{\phi}$ as the upstream depth-averaged particle concentration (i.e. $\bar{\phi}^{exp}$) for both the bulk suspension and large-particle component, respectively.

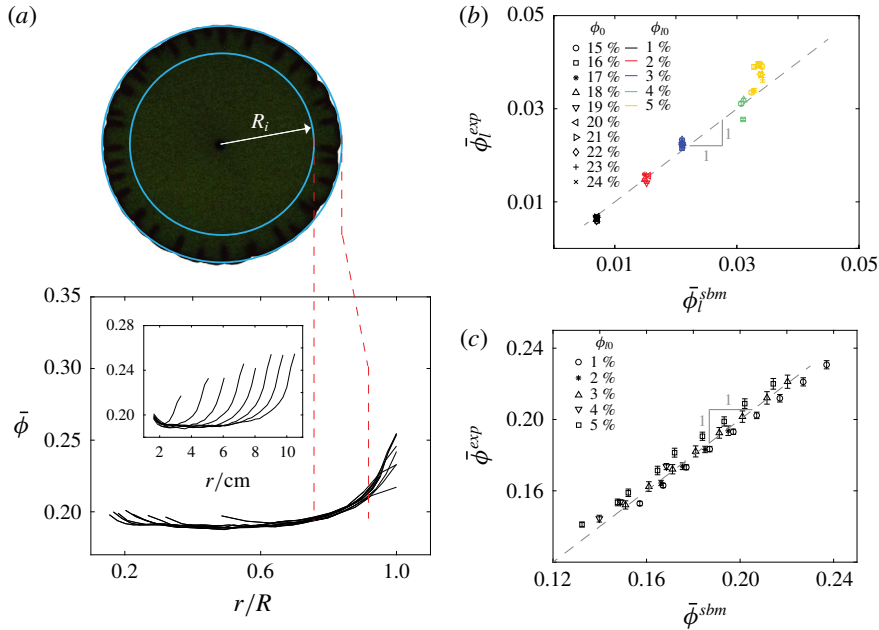


FIGURE 8. (Colour online) (a) The depth-averaged concentration profiles acquired from experimental measurements collapse onto a single curve when normalised by the radius of the corresponding fitted circle R . We thus argue that the upstream region corresponds to the relatively flat portion of the collapsed curve of $\bar{\phi}$, whose boundary is further defined as R_i . (b,c) Plots comparing the experimental measurements of $\bar{\phi}_l$ and $\bar{\phi}$ with the theoretical prediction show reasonable agreement.

Figure 8(b,c) shows the plots of $\bar{\phi}^{exp}$ versus $\bar{\phi}^{sbm}$, the upstream depth-averaged concentrations from the simplified model, for all values of ϕ_0 and ϕ_{l0} considered. For both total and large-particle concentrations upstream, the agreement between experiments and theory is reasonable, shown by their close collapse onto a line with slope of 1. However, given the breakdown of the continuum assumption and the discontinuity at $z = 0$ (see figure 7a), the model is not expected to fully resolve the details of concentration profiles in z . Despite these limitations, the agreement between theory and experiments in $\bar{\phi}$ demonstrates the usefulness of our reduced equilibrium model.

With the upstream theoretical model verified against experimental data, we now address one of the key observations of the bidisperse experiments – the preferential accumulation of large particles on the interface. As the amount and rate of particles injected into the cell are fixed, the accumulation of particles on the interface must be met by the depletion of particles from the upstream regime, or $\bar{\phi} < \phi_0$ for $0 < r < R_i(t)$. In particular, the value of upstream $\bar{\phi}_l$ relative to ϕ_{l0} directly informs the depletion of large particles from the upstream and, thereby, their accumulation near the interface. Figure 9(a) shows the plot of $\bar{\phi}_l$ versus ϕ_{l0} for $\phi_0 = 20\%$ both from experiments (triangle) and from the suspension balance model (solid line). A dashed line of slope 1 is included to visually showcase the deviation of $\bar{\phi}_l$ from ϕ_{l0} , which clearly grows with ϕ_{l0} . This indicates that an increase in ϕ_{l0} directly increases the accumulation of large particles on the interface. Also, the same trend is evident experimentally for all values of ϕ_0 , as shown in the inset of figure 9(a). On the other hand, figure 9(b)

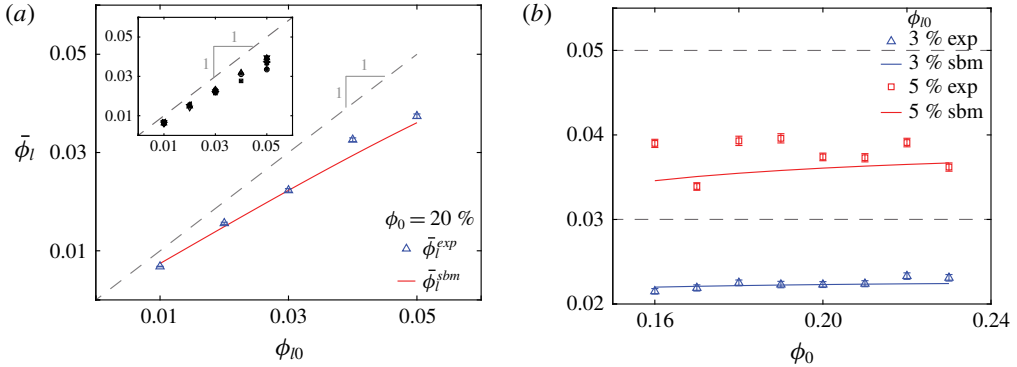


FIGURE 9. (Colour online) (a) Plots of $\bar{\phi}_l$ from both experimental measurements and theoretical prediction with respect to ϕ_{l0} at $\phi_0 = 20\%$. The observation that $\bar{\phi}_l$ falls below the auxiliary curve of slope 1 clearly indicates the occurrence of preferential accumulation of large particles near the interface. The inset shows all experimental measurements of $\bar{\phi}_l$ against ϕ_{l0} , suggesting the trend is true for all experiments. (b) Plot of $\bar{\phi}_l$ against ϕ_0 for $\phi_{l0} = 3\%$ and 5% . All data points fall below the auxiliary lines of their corresponding ϕ_{l0} , again confirming our observation of the preferential accumulation of large particles at the interface. Here, $\bar{\phi}_l$ appears to be independent of ϕ_0 .

shows that $\bar{\phi}_l$ is mostly independent of ϕ_0 for $\phi_{l0} = 3\%$ and 5% , respectively, for both experiments (symbols) and theory (solid line).

As illustrated in figure 9, our reduced model successfully captures the trend in $\bar{\phi}_l$ with ϕ_0 and ϕ_{l0} and can help rationalise the preferential accumulation of large particles on the interface. For instance, the model assumes that small particles remain uniformly distributed in the suspension, while the large particles migrate to the channel centre under shear-induced diffusion. Therefore, any particle accretion on the interface, or depletion from upstream, can only directly come from ϕ_{l0} . An increase in $\phi_{l0} - \bar{\phi}_l$ with ϕ_{l0} naturally follows from this model assumption. In addition, our model predicts that, for given ϕ_{l0} , increasing ϕ_0 (or ϕ_{s0}) only acts to enhance the background viscosity. As the shear-induced migration of large particles should be independent of the background viscosity, this explains why $\bar{\phi}_l$ does not depend on ϕ_0 . Overall, as previously hypothesised, the suppression of shear-induced migration of small particles and their uniform distribution are central to the notable accretion of large particles near the interface.

Finally, based on mass conservation, the total particle volume that collects near the interface can be approximated by the difference between the total particle volume at time t , $\phi_0 \pi R(t)^2 h$, and that inside the upstream regime, $\bar{\phi} \pi R_i(t)^2 h$. Normalising by $\pi R(t)^2 h$ yields the following expression for the dimensionless amount of particles that have accumulated near the interface:

$$V^p \equiv \phi_0 - \bar{\phi} \left(\frac{R_i}{R} \right)^2, \tag{3.14}$$

which is independent of time; it is straightforward to compute the value of V^p from the experiments for all ϕ_0 and ϕ_{l0} . Interestingly, the V^p dependence on ϕ_{l0} comes most directly from R_i/R . Figure 10(a) shows that R_i/R monotonically decreases with ϕ_{l0} , independent of ϕ_0 . Qualitatively, this implies that the addition of large particles

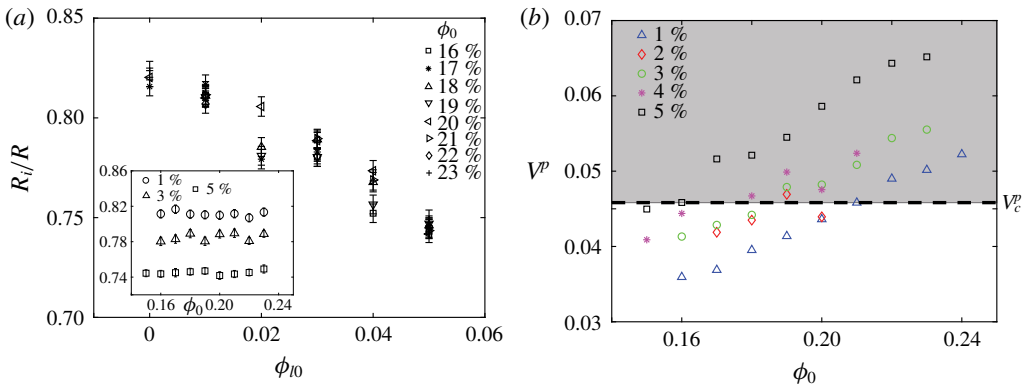


FIGURE 10. (Colour online) (a) The ratio of R_i/R is plotted against ϕ_{10} for all experiments available. The measurements of corresponding monodisperse experiments are also included here for comparison. The ratio appears to decrease monotonically with ϕ_{10} but is independent of ϕ_{10} as depicted by the inset. (b) Plot of V^p with respect to ϕ_0 , where each colour represents a different value of ϕ_{10} . The region above the critical value 0.45 is shaded in grey and almost all data points therein correspond to the ‘fingering’ regime.

expedites the particle accumulation (or shortens R_i). Similarly, the inclusion of large particles was shown to expedite the time of fingering onset in § 2.3.3. While we conjecture that both expedited accumulation and fingering may be related to the time scale of particle migration, the quantitative analysis remains outside the scope of the current paper.

Plotting V^p from data in terms of ϕ_0 for varying ϕ_{10} reveals another surprising feature (see figure 10b). The values of ϕ_0 and ϕ_{10} at which fingering initiates (see the phase diagram in figure 5) happen to fall on approximately a constant value of V^p , i.e. $V_c^p \approx 0.45$. Alternatively, the values of ϕ_0 and ϕ_{10} for which $V^p \gtrsim V_c^p$ yield fingering in the current experimental time scale, while those for which $V^p < V_c^p$ are in the ‘no fingering’ regime. Consistent with Xu *et al.* (2016), the existence of V_c^p itself suggests that the critical onset of fingering depends on the total amount of particles that accumulate on the interface, which will be explored in future studies.

4. Discussion

In this paper, we experimentally demonstrate that the previously reported particle-induced fingering for monodisperse suspensions (Tang *et al.* 2000; Xu *et al.* 2016; Kim *et al.* 2017) can be enhanced by introducing a second species of particles with larger diameter. The experiments are performed by injecting a bidisperse suspension at a constant flow rate Q into a Hele-Shaw cell to displace air. The mixture consists of viscous silicone oil and non-colloidal neutrally buoyant particles with two distinct diameters, d_l and d_s , where $d_l/d_s \sim 2-3$; the key experimental parameters are the initial total particle volume fraction ϕ_0 and initial large-particle concentration ϕ_{10} . As we are mainly interested in the potentially significant effects that even the small addition of large particles can have on fingering, ϕ_{10} never exceeds 5% and is always below ϕ_{s0} by a factor of 2 or more.

Two series of experiments are conducted by systematically varying ϕ_0 at fixed ϕ_{10} , or by modulating ϕ_{10} at given ϕ_0 . Using image processing tools and the ANN, we then extract the depth-averaged particle concentrations inside the suspension and

the deformation of the suspension–air interface. Consistent with previous results, an increase in ϕ_0 appears to induce fingering and lead to larger interfacial deformations regardless of ϕ_{l0} . However, there are two noteworthy results that are directly due to the inclusion of larger particles. First, despite the relatively small amount present in the suspension, large (red) particles are observed to consistently enrich the expanding fluid–fluid interface, in lieu of more prevalent small (green) particles. Second, for given ϕ_0 , increasing ϕ_{l0} expedites the onset of fingering and, hence, shifts the transition between ‘fingering’ and ‘no fingering’ regimes.

The key to particle-induced fingering is the accumulation of particles on the interface, which generates the destabilising viscosity gradient for miscible viscous fingering. Therefore, understanding the mechanism of particle accumulation must precede the characterisation of fingering dynamics at the interface. Accordingly, we use the reduced model based on the suspension balance approach (Nott & Brady 1994; Norman *et al.* 2008) to rationalise the particle accumulation of bidisperse suspensions due to shear-induced migration (Graham *et al.* 1991; Husband *et al.* 1994; Chow *et al.* 1995; Lyon & Leal 1998*b*). The model is used to describe the quasi-fully developed flow far upstream of the interface, where equilibrium assumptions are appropriate (Murisic *et al.* 2013). By assuming a uniform distribution of small particles, as evident in both our data and those of Lyon & Leal (1998*b*), the particle concentration and velocity profiles are numerically calculated as a function of z . We also compute the depth-averaged concentrations of large particles in satisfactory agreement with the experimental data. The model results suggest that the suppression of shear-induced migration of small particles upstream drives the preferential accumulation of large particles at the meniscus and enhanced fingering.

This combined experimental and theoretical study builds on the previous study of particle-induced viscous fingering of monodisperse suspensions and is the first of its kind to demonstrate the role of polydispersity on fingering. Future work includes understanding the existence of the critical particle volume V_c^p that is connected to fingering, as well as deriving a theoretical model for the onset radius of accumulation, R_i/R , as a function of ϕ_{l0} . The present work could also be strengthened by widening the experimental parameter space, for instance, by modulating flow rates, including more than two particle types, or even changing the channel geometry. Finally, the key point to take away from the current study is that any small changes to the particle mixture that changes shear-induced migration can make a huge difference in fingering phenomena. Therefore, another exciting direction of future research lies in finding other seemingly ‘small’ ways of dramatically changing the particle-induced viscous fingering, such as the inclusion of non-spherical particles or particles of varying rigidity that alter shear-induced migration.

Appendix A. Pseudo-code for artificial neural network

In addition to the symbols introduced in §2.2, we further define δ as the error vector, which is the difference between the classification vector and the output of the network in each iteration, $\mathbf{\Delta}$ and \mathbf{D} are matrices used to store the coefficients in the process of back-propagation, and ξ represents a constant chosen empirically. The pseudo-code is given as follows:

- (1) Get the training set $(x^{(1)}, y^{(1)}), \dots, (x^{(m)}, y^{(m)})$
- (2) Set $\Delta_{ij}^{(l)} = 0$ for all l, i, j
- (3) For $i = 1$ to m
 - (i) Set $a^{(1)} = x^{(i)}$

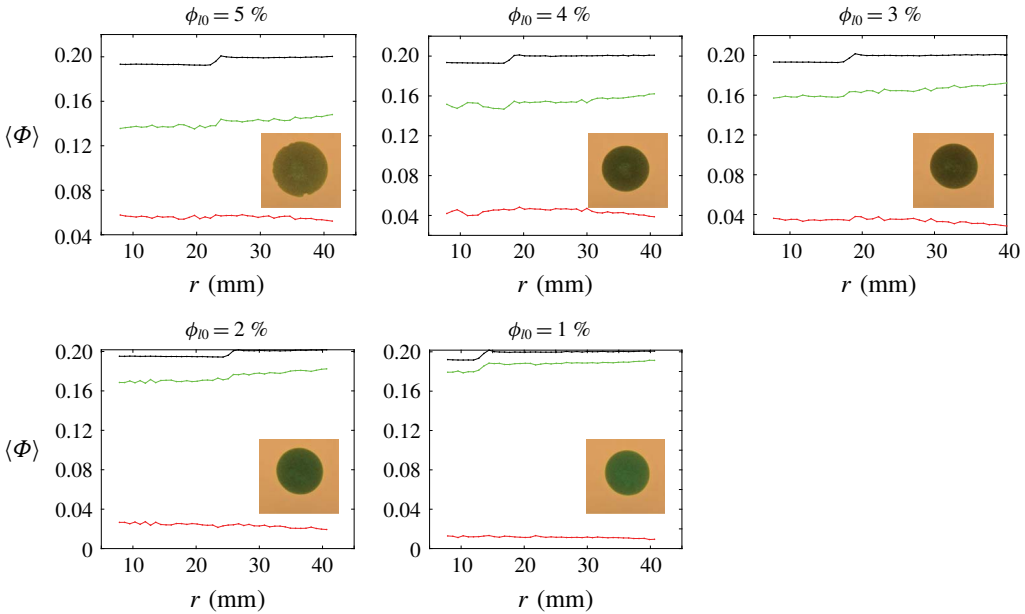


FIGURE 11. (Colour online) Plots of the depth-averaged concentration profiles ($\bar{\phi}$ (black), $\bar{\phi}_s$ (green) and $\bar{\phi}_l$ (red)) as functions of radial position r for stationary bidisperse mixtures that are placed on a glass plate. All five samples have $\phi_0 = 20\%$, while ϕ_{10} is varied from 1% to 5% by an increment of 1%.

- (ii) Perform forward propagation to compute $a^{(l)}$ for $l = 2, 3, \dots, L$: $a^{(l)} = g(W^{(l-1)}a^{(l-1)})$
- (iii) Using $y^{(i)}$, compute $\delta^{(L)} = a^{(L)} - y^{(i)}$
- (iv) Compute $\delta^{(L-1)}, \delta^{(L-2)}, \dots, \delta^{(2)}$
- (v) $\Delta_{ij}^{(l)} := \Delta_{ij}^{(l)} + a_j^{(l)} \delta_i^{(l+1)}$
- (4) $D_{ij}^{(l)} := (1/m)\Delta_{ij}^{(l)} + \xi W_{ij}^{(l)}$ if $j \neq 0$
- (5) $D_{ij}^{(l)} := (1/m)\Delta_{ij}^{(l)}$ if $j = 0$

By the end of the algorithm, we have $(\partial/\partial W_{ij}^{(l)})J(\mathbf{W}) = D_{ij}^{(l)}$, which contains the desired coefficients of the network.

Appendix B. Calibration results for artificial neural network

For calibration purposes, the ANN method has been applied to a series of bidisperse samples with known concentrations, namely $\phi_{10} = 1\% - 5\%$, while ϕ_0 is fixed at 20%. The samples are prepared by carefully measuring out each component (i.e. large (red) and small (green) particles) and mixing them thoroughly in oil, before they are placed onto a plate and imaged from directly above. We then compute the depth-averaged particle concentrations using the ANN method and plot them against the radial position r in figure 11. The results exhibit the average deviation of $\Delta = 0.75\%$, 2.87% and 3.34% for ϕ_0 , ϕ_{s0} and ϕ_{l0} , respectively, where $\Delta = 100\% |\bar{\phi}^{ANN} - \phi_0|/\phi_0$. Overall, the calibration results demonstrate that the ANN technique effectively produces physically meaningful values of depth-averaged particle concentrations in the current set-up.

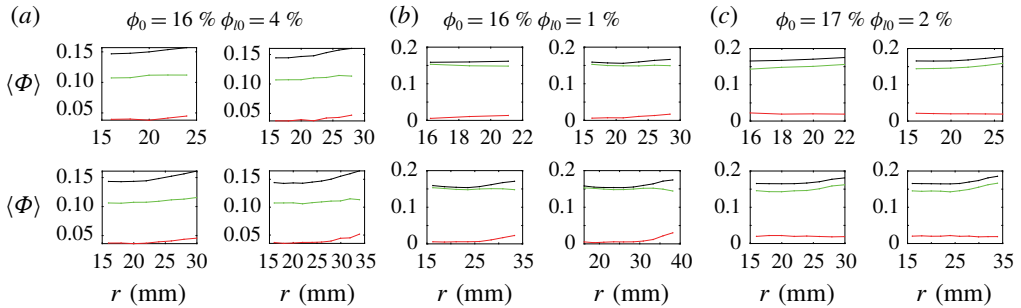


FIGURE 12. (Colour online) Plots of the depth-averaged concentration profiles ($\bar{\phi}$ (black), $\bar{\phi}_s$ (green) and $\bar{\phi}_l$ (red)) over r at early times. The top-left plot in each panel corresponds to the earliest time, and time then evolves clockwise.

Appendix C. Particle concentrations at early times

Here, we include the plots of the depth-averaged particle concentrations, i.e. $\bar{\phi}$ (black), $\bar{\phi}_s$ (green) and $\bar{\phi}_l$ (red), at early times (around $r = 2$ cm) for three concentration combinations. Each panel in figure 12 contains four plots that show progression in time (starting with the top-left plot and going clockwise). A slight increase in $\bar{\phi}$ in the top-left subplot indicates that particles might have enriched the meniscus inside the injection tube, prior to entering the Hele-Shaw cell.

REFERENCES

- ALPADYDIN, E. 2009 *Introduction to Machine Learning*, 2nd edn. MIT Press.
- ALTOBELLI, S. A. & MONDY, L. A. 2002 Hindered flotation functions from nuclear magnetic resonance imaging. *J. Rheol.* **46**, 1341–1352.
- BECKWITH, T. G. & MARANGONI, R. D. 1993 *Mechanical Measurements*, 5th edn. Addison-Wesley.
- BEYEA, S. D., ALTOBELLI, S. A. & MONDY, L. A. 2003 Chemically selective NMR imaging of a 3-component (solid–solid–liquid) sedimenting system. *J. Magn. Resonance* **161**, 198–203.
- BOYER, F., GUAZZELLI, E. & POULIQUEN, O. 2011 Unifying suspension and granular rheology. *Phys. Rev. Lett.* **107**, 188301.
- CHAHAL, D., AHMADI, A. & CHEUNG, K. C. 2012 Improving piezoelectric cell printing accuracy and reliability through neutral buoyancy of suspensions. *Biotechnol. Bioengng* **109** (11), 2932–2940.
- CHAPMAN, B. K. 1990 Shear-induced migration phenomena in concentrated suspensions. PhD thesis, University of Notre Dame.
- CHOW, A. W., HAMLIN, R. D. & YLITALO, C. M. 1995 Size segregation of concentrated bidisperse and polydisperse suspension during tube drawing. In *IUTAM Symposium on Hydrodynamic Diffusion of Suspended Particles*, pp. 45–50. Colorado University, Boulder, CO.
- CONNELL, J. L., RITSCHDORFF, E. T., WHITELEY, M. & SHEAR, J. B. 2013 3D printing of microscopic bacterial communities. *Proc. Natl Acad. Sci. USA* **110** (46), 18380–18385.
- DAGOIS-BOHY, S., HORMOZI, S., GUAZZELLI, E. & POULIQUEN, O. 2015 Rheology of dense suspensions of non-colloidal spheres in yield-stress fluids. *J. Fluid Mech.* **776**, R2.
- GRAHAM, A. L., ALTOBELLI, S. A., FUKUSHIMA, E., MONDY, L. A. & STEPHEN, T. S. 1991 Note: NMR imaging of shear-induced diffusion and structure in concentrated suspensions undergoing Couette flow. *J. Rheol.* **135**, 191–201.
- HOMSY, G. M. 1987 Viscous fingering in porous media. *Annu. Rev. Fluid Mech.* **19**, 271–311.
- HUSBAND, D. M., MONDY, L. A., GANANI, E. & GRAHAM, A. L. 1994 Direct measurements of shear-induced particle migration in suspensions of bimodal spheres. *Rheol. Acta* **33**, 185–192.
- KARNIS, A. & MASON, S. G. 1967 The flow of suspensions through tubes. IV. Meniscus effects. *J. Colloid Interface Sci.* **23**, 120–133.

- KIM, J., XU, F. & LEE, S. 2017 Formation and destabilization of the particle band on the fluid–fluid interface. *Phys. Rev. Lett.* **118**, 074501.
- VAN DER KOOIJ, F. M., KASSAPIDOU, K. & LEKKERKERKER, H. N. W. 2000 Liquid crystal phase transitions in suspensions of polydisperse plate-like particles. *Nature* **406**, 868–871.
- KRISHNAN, G. & LEIGHTON, D. T. 1994 Shear-induced size segregation phenomena in bidisperse suspensions. *Appl. Mech. Rev.* **47** (6), S236–S239.
- KRISHNAN, G. P., BEIMFOHR, S. & LEIGHTON, D. T. 1996 Shear-induced radial segregation in bidisperse suspensions. *J. Fluid Mech.* **321**, 371–393.
- LECAMPION, B. & GARAGASH, D. I. 2014 Confined flow of suspensions modelled by a frictional rheology. *J. Fluid Mech.* **759**, 197–235.
- LEE, S., STOKES, Y. & BERTOZZI, A. 2014 Behavior of a particle-laden flow in a spiral channel. *Phys. Fluids* **26**, 043302.
- LEIGHTON, D. & ACRIVOS, A. 1987a Measurement of shear-induced self-diffusion in concentrated suspensions of spheres. *J. Fluid Mech.* **177**, 109–131.
- LEIGHTON, D. & ACRIVOS, A. 1987b The shear-induced migration of particles in concentrated suspensions. *J. Fluid Mech.* **181**, 415–439.
- LYON, M. K. & LEAL, L. G. 1998a An experimental study of the motion of concentrated suspensions in two-dimensional channel flow. Part 1. Monodisperse systems. *J. Fluid Mech.* **363**, 25–56.
- LYON, M. K. & LEAL, L. G. 1998b An experimental study of the motion of concentrated suspensions in two-dimensional channel flow. Part 2. Bidisperse systems. *J. Fluid Mech.* **363**, 57–77.
- MORRIS, J. F. & BOULAY, F. 1999 Curvilinear flows of noncolloidal suspensions: the role of normal stress. *J. Rheol.* **43**, 1213–1237.
- MORRIS, J. F. & BRADY, J. F. 1998 Pressure-driven flow of a suspension: buoyancy effects. *Intl J. Multiphase Flow* **24**, 105–130.
- MURISIC, N., HO, J., HU, V., LATTEMAN, P., KOCH, T., LIN, K., MATA, M. & BERTOZZI, A. 2011 Particle-laden viscous thin-film flows on an incline: experiments compared with a theory based on shear-induced migration and particle settling. *Physica D* **240** (20), 1661–1673.
- MURISIC, N., PAUSADER, B., PESCHKA, D. & BERTOZZI, A. L. 2013 Dynamics of particle settling and resuspension in viscous liquid films. *J. Fluid Mech.* **717**, 203–231.
- NORMAN, J. T., OGUNTADE, B. O. & BONNECAZE, R. T. 2008 Particle-phase distributions of pressure-driven flows of bidisperse suspensions. *J. Fluid Mech.* **594**, 1–28.
- NOTT, P. R. & BRADY, J. F. 1994 Pressure-driven flow of suspensions – simulation and theory. *J. Fluid Mech.* **275**, 157–199.
- RAMACHANDRAN, A. & LEIGHTON, D. T. 2007 The effect of gravity on the meniscus accumulation phenomenon in a tube. *J. Rheol.* **51** (5), 1073–1098.
- RAMACHANDRAN, A. & LEIGHTON, D. T. 2010 Particle migration in concentrated suspensions undergoing squeeze flow. *J. Rheol.* **54**, 563–589.
- SAFFMAN, P. G. & TAYLOR, G. 1958 The penetration of a fluid into porous medium or Hele-Shaw cell containing a more viscous liquid. *Proc. R. Soc. Lond. A* **245**, 312–329.
- SHAN, Y., NORMAND, M. & PELEG, M. 1997 Estimation of the surface concentration of adhered particles by colour imaging. *Powder Technol.* **92**, 147–153.
- SHAPIRO, A. P. & PROBSTEIN, R. F. 1992 Random packings of spheres and fluidity limits of monodisperse and bidisperse suspensions. *Phys. Rev. Lett.* **68**, 1422–1425.
- SHAULY, A., WACHS, A. & NIR, A. 1998 Shear-induced particle migration in a polydisperse concentrated suspension. *J. Rheol.* **42**, 1329–1348.
- SNOOK, B., BUTLER, J. E. & GUZZELLI, E. 2016 Dynamics of shear-induced migration of spherical particles in oscillatory pipe flow. *J. Fluid Mech.* **786**, 128–153.
- STORMS, R. F., RAMARAO, B. V. & WEILAND, R. H. 1990 Low shear rate viscosity of bimodally dispersed suspensions. *Powder Technol.* **63**, 247–259.
- TANG, H., GRIVAS, W., HOMENTCOVSKI, D., GEER, J. & SINGLER, T. 2000 Stability considerations associated with the meniscoid particle band at advancing interfaces in Hele-Shaw suspension flow. *Phys. Rev. Lett.* **85**, 2112–2115.
- XU, F., KIM, J. & LEE, S. 2016 Particle-induced viscous fingering. *J. Non-Newtonian Fluid Mech.* **238**, 92–99.